DOI: 10.1109/TASC.2021.3061352
FERMILAB-PUB-21-126-TD
(accepted)

Progress in the Development of the Nb_3Sn MQXFB Quadrupole for the HiLumi Upgrade of the LHC

Susana Izquierdo Bermudez ; Giorgio Ambrosio ; Giorgio Apollinari; Marta Bajko ; Bernardo Bordini ; Nicolas Bourcey ; Delio Duarte Ramos, Paolo Ferracin ; Lucio Fiscarelli ; Sandor Feher; Jerome Fleiter ; Michael Guinchard ; Friedrich Lackner ; Nicholas Lusa; Franco Mangiarotti ; Attilio Milanese; Rosario Principe, Juan Carlos Perez ; Herve Prin ; Dariusz Pulikowski; Eelis Tapani Takala; Emmanuele Ravaioli ; Ezio Todesco

***Abstract*—. The high-luminosity upgrade of the Large Hadron Collider (HL-LHC) requires new high field and large-aperture quadrupole magnets for the low-beta inner triplets (MQXF). With a nominal operating gradient of 132.2 T/m in a 150 mm aperture and a conductor peak field of 11.3 T, the new quadrupole magnets are based on Nb_3Sn superconducting technology. After a series of short models constructed in close collaboration by LARP (LHC Accelerator Research Program) and CERN, the development program is entering in the series production phase with CERN on one side and the US Accelerator Upgrade Project (US-AUP) on the other side assembling and testing full-length magnets. This paper describes the status of the development activities at CERN, in particular on the cold powering test of the first MQFXB prototype and on the construction of the second full scale prototype. Critical operations such as reaction heat treatment, coil impregnation and magnet assembly are discussed. Finally, the plan towards the series production is described**

***Index Terms*— High Luminosity LHC, Nb_3Sn magnets**

I. Introduction

With the High Luminosity Upgrade of the Large Hadron Collider (HL-LHC), CERN is planning to upgrade the interaction region in order to increase the peak luminosity by a factor 2 and the integrated luminosity by a factor 10 [1]. Since the beam size in the Interaction Point (IP) is inverse proportional to the aperture of the first magnets after the experiments, the HL-LHC project requires the replacement of the Interaction Region (IR) magnets with larger aperture ones [2]. An essential ingredient of the IR magnets upgrade is the triplet, that is the sequence of the first three quadrupoles (Q1, Q2a, Q2b and Q3) in front of the experiments. With respect to the current triplet quadrupoles, the new magnets called MQXF ([3],[4]), will feature a larger aperture, from 70 to 150 mm, a higher peak field, from 8.6 to 11.2 T, and a new superconducting material, Nb_3Sn instead of Nb-Ti. The magnetic length of Q1/Q3 is 8.4 m, split in two magnets of 4.2 m (MQXFA) which are being fabricated by the US Accelerator Research Program (AUP) [5], a continuation of the LARP (LHC Accelerator Research Program [6]. CERN is in charge of MQXFB, the 7.2 m long magnets that will be inserted in a single cold mass for the Q2a and Q2b. MQXFA and MQXFB have identical cross-sections (see Fig. 1) and 3D design. After a series of short models constructed in close collaboration by LARP and CERN [7], the development program is entering in the series production phase assembling and testing full-length magnets. Here we give an update of the cold powering test results of the first MQXFB prototype (MQXFBP1), the construction activities of the second prototype (MQXFBP2) and the plans towards series production.

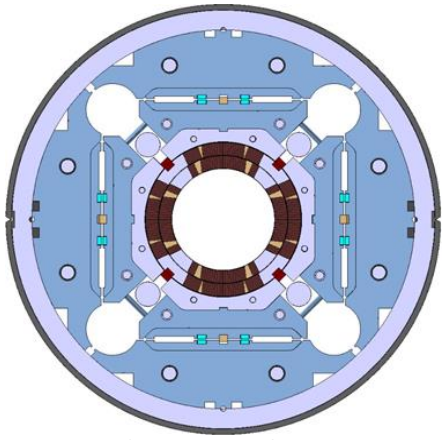

Fig. 1. Cross-section of the Nb_3Sn low-β quadrupole magnet MQXF

II. Superconducting Strand And Cable

MQXF coils are made with a Rutherford-type cable composed of 40 strands of 0.85 mm diameter. The cable incorporates a 12 mm wide 25 μm thick stainless-steel core to reduce inter-strand coupling currents. RRP 108/127 strands from Bruker will be used for all MQXFB series magnets. CERN also supported an effort to develop a second technology, namely the PIT strand by Bruker-OST, with 192 subelements [8]. It has been used for the construction of two short models and five MQXFB coils. 9.1 tons of RRP 108/127 and 3.3 tons of bundle-barrier 192 PIT have been received and accepted by CERN. The remaining quantity to fulfill the production, 1.7

Manuscript received XX;

Susana Izquierdo Bermudez ; Marta Bajko ; Bernardo Bordini ; Nicolas Bourcey ; Delio Duarte Ramos,; Lucio Fiscarelli Jerome Fleiter ; Michael Guinchard ; Friedrich Lackner ; Nicholas Lusa; Franco Mangiarotti ; Attilio Milanese; Rosario Principe, Juan Carlos Perez ; Herve Prin ; Dariusz Pulikowski; Eelis Tapani Takala; Emmanuele Ravaioli ; Ezio Todesco are with CERN, CH-1211 Geneva 23, Switzerland (e-mail: susana.izquierdo.bermudez@cern.ch).

P. Ambrosio, G. Apollinari and S. Feher are with Fermi National Accelerator Laboratory (FNAL), Batavia, IL 60510 USA.

P. Ferracin is with Lawrence Berkeley National Laboratory (LBNL), Berkley, CA 94720 USA.

Color versions of one or more of the figures in this paper are available online at http://ieeexplore.ieee.org.

Digital Object Identifier

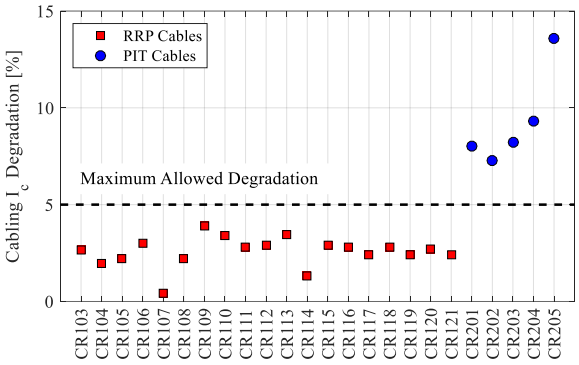

Fig. 2. Average critical current density degradation due to cabling.

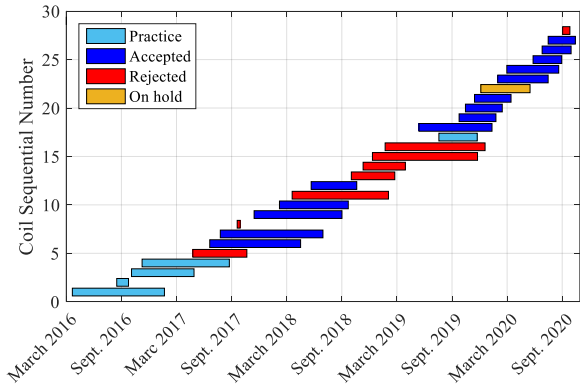

Fig. 3. MQXFB coil production dashboard.

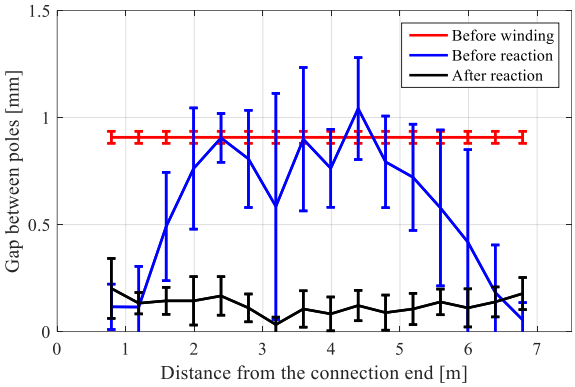

Fig. 4. Average (and std) gap between segments before winding, after relaxing the winding tension and after reaction for RRP coils.

tons of RRP 108/127, are expected to be delivered by summer 2021 [9].

In total, 31 MQXFB cables have been produced up to date, with one rejected due to a strand cross-over [10]. A second cable is on hold due to abnormal deformation of the stainless-steel core. The design assumes a critical current degradation due to cabling of 5 %. The average degradation of the RRP cables is 3 % (see Fig. 2), whereas in the PIT cables the degradation is 7-14 % [11]. The cable is insulated with braided S2 glass, with a target thickness at 5 MPa of 0.145 mm [12].

III. Coil Fabrication

MQXF coil fabrication is based on the wind-and-react technology where the superconducting phase is formed after winding and during coil heat treatment. Both short coils and MQXFA coils were fabricated using two different cable designs: a 1st generation cable with keystone angle of 0.55°, and a 2nd generation cable, where the angle was decreased to 0.40° to reduce the critical current degradation due to cabling [13]. All MQXFB coils were fabricated with the 2nd generation cable. To correct the systematic b_6 measured in the first short models and MQXFA magnets, a second modification on the cross section took place during the coil fabrication. Starting from coil CR202, pole insulation thickness was increased by 0.125 mm, decreasing the mid-plane thickness by the same amount. Using this approach, the azimuthal turn position can be optimized without an impact on the coil compaction during reaction.

A. Coil production

The production of MQXFB coils started in 2016 with two copper coils followed by two low performance Nb_3Sn RRP conductor (CR001, CR002, CR101 and CR102) [14]. In spring 2017, the production of the coils for the first prototype started (CR104-CR109)[15]. Following a series of critical nonconformities (see Fig. 3, red bars), coil fabrication was on hold the first half of 2019 to review manufacturing procedures and improve the robustness of the process. In September 2019 coil fabrication resumed, with a production flow of approximately one coil per month. From September 2019, ten conformed coils have been produced, one is on-hold and one was rejected due to a critical nonconformity during winding. Four out of the five PIT coils were rejected so the analysis on coil fabrication focus only on RRP coils.

B. Winding, Curing, Reaction, Impregnation

The cable is wound around a titanium pole keeping a tension on the cable of 19 kg in the straight section and 7 kg in the ends. Gaps are placed between pole segments to allow the coil to contract in the longitudinal direction from the winding tension and from the conductor contraction during heat. The goal is to have the gaps closed after reaction. The initial assumed length of contraction was 17.6 mm (2.5 mm/m) distributed over 16 gaps. After the production of 5 coils, the total pole gap was reduced to 14.4 mm. Figure 4 shows the measured average and standard deviation of the pole gap. After releasing the winding tension, the gap between poles decreases mostly in the coil ends. After reaction, poles gaps are almost closed. After the first layer is wound, polymer-derived ceramic binder CTD-1202 ($\sim$ 60 g/m) is applied to the S2 glass insulation of the cables; the binder is then cured in two steps, first at 80 °C for 1.5 h, then at 160 °C for 3 h. The same operation is applied to the second layer, after its winding on top of the first one to obtain a compact coil. Once the winding and curing are completed, the coil is placed in a reaction mold and heat treated in an oven under argon flow to form Nb_3Sn. The reaction process requires three plateaus at 210 ºC, 400 ºC and 665 ºC. To improve Residual Resistivity Ratio (RRR) and guarantee a minimum of 100, the duration of the last plateau

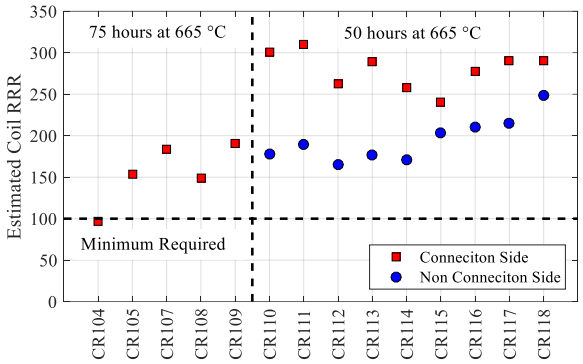

Fig. 5. Estimated coil RRR based on samples reacted with the coil. The vertical line indicates the change of duration of the last plateau during reaction.

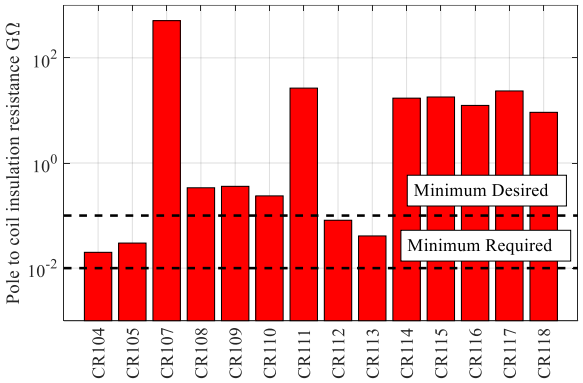

Fig. 6. Pole to coil electrical insulation after impregnation.

was decreased from 75 hours to 50 hours. Figure 5 shows that, thanks to the reduction of the heat treatment time, the RRR measured in witness samples reacted with the coil increased by 100 in average. From coil CR110, samples were included in the coil non-connection side (outlet of the argon flow) showing a significant degradation of the RRR. Thanks to an improvement on the leak-tightness of the reaction fixture, the difference in RRR among the connection and non-connection side decreased significantly in the last coils.

Before transferring the reacted coil in the impregnation mold, a flexible circuit which includes quench protection heaters is installed in the coil outer radius. Nb-Ti leads are also soldered to the Nb_3Sn cable before impregnation, using $Sn_{96}Ag_4$ as solder and halide free flux. The coil is closed in the impregnation mold and CTD-101 K resin is injected at 60 ºC inside a vacuum tank. In order to achieve a good level of vacuum in the mould prior to injection, the mould is heated to 110 °C and flushed several times with nitrogen. It is then cooled down to 60 °C, and evacuated, for resin injection[16]. The typical injection time is 3 hours. The epoxy curing is done at 2 bars pressure in two plateaus, the first at 110 °C for 5 h and the second at 125 °C for 16 h.

C. *Electrical tests*

Each production step is followed by an electrical qualification test [15]. The final acceptance of the coil is based on the electrical tests after impregnation. The quality of the interturn insulation is verified applying a 2.5 kV discharge in the coil.

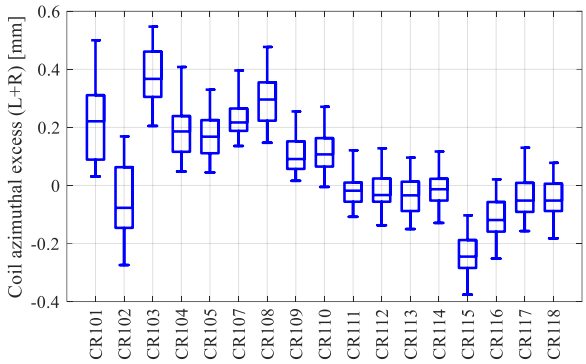

Fig. 7. Azimuthal coil size deviation (left + right mid-plane) with respect to nominal dimension for MQXFB RRP coils.

In addition, insulation coil to quench heaters and coil to ground is verified to a level of 3.7 kV [17]. One of the critical parameters on the MQXFB coil construction is the insulation coil to pole. The pole is floating, and the maximum voltage drop during quench in the pole turns is 10 V meaning that 10 MΩ resistance between coil and pole is considered sufficient to assure safe operation. Figure 6 shows the measured insulation resistance to the pole after impregnation. Thanks to a series of improvements in the coil fabrication process, the pole to coil insulation is above 1 GΩ for the last 5 coils.

D. *Coil metrology*

After impregnation, each coil is measured in 43 longitudinal cross sections, using the coil outer diameter and pole keyway as alignment for the CMM best fit to reproduce the functional magnet configuration [18]. In Fig. 7, the azimuthal deviations (left + right mid-plane) of each coil with respect to nominal dimensions are given in the form of a box plot: the horizontal lines indicate the minimum, the 25% percentile, the median, the 75% percentile, and the maximum deviations. The size variation along the straight section length stabilized in the last 10 coils to ± 0.125 mm. The median ranges from + 0.40 mm to -0.30 mm. Coil CR111 to CR114 were impregnated using the same set of radial fillers and mid-plane shims and have an azimuthal size close to nominal. Thicker (out of tolerance) mid-plane shims and radial fillers were used for CR115, resulting in a coil azimuthal size 0.250 mm smaller than nominal. This was corrected from coil 116 by using mid-plan shims with the nominal size. The total coil length is 7493 ± 5 mm, 12 mm longer in average that the nominal coil length (7481 mm). Most of the deviation is coming from the coil ends.

IV. Magnet Assembly And Loading

Uniform pre-load and field homogeneity require precise coil positioning and alignment during assembly. The nominal outer radius of the MQXF coils is equal to 113.376 mm, 0.625 mm smaller than the collars inner radius. This gap can be filled with radial polyimide shims, in the configuration shown in Fig. 8. One 125 μm polyimide layer is wrapped around the coil, and two around the collars, with a total thickness of 375 μm which constitute the ground plane insulation. Two ad-

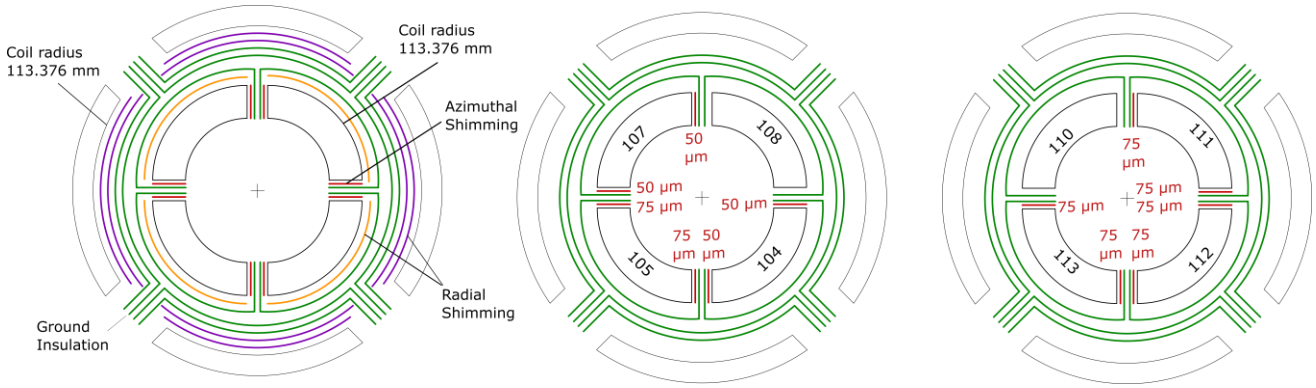

Fig. 8. Standard shimming applicable for the MQXF magnets (left). Shimming plan and coil positioning adopted for MQXFBP1 (middle) MQXFBP2 (right).

ditional layers are foreseen to match the nominal coil radius to the collar one, allowing to accommodate oversized coils. Using as input the measured average coil azimuthal size, full-length polyimide sheets are installed on the coils' mid-planes and/or on the outer radius surfaces, so that the final average radial and azimuthal envelope of the four shimmed coils coincide. The azimuthal solution is in general preferred, as it allows to bring the four coils inner surface at the same radius, with beneficial effects on the field homogeneity [19]. Radially, the target is to have about 125 μm smaller shims in order to improve the coil-collar contact [20]. Figure 8 shows the final shimming lay-out for the two MQXFB Prototype magnets. The coil pack radial size is 60 μm and 150 μm smaller than nominal in MQXFBP1 and MQXFBP2, respectively.

The assembly of the MQXF structure is described in detailed in [21]-[26]. The MQXFBP1 and MQXFBP2 preloading follows the same four step procedure as the latest short models and MQXFA magnets: 1) half of the azimuthal load; 2)half of the axial load; 3) full azimuthal load and 4). full axial load. The axial loading is applied by symmetrically increasing tension in the end plate rods (bolt tightening with a help of a piston) while at the same time observing the rod strains and elongations. The longitudinal prestress at warm in MQXFBP1 was equal 0.6 MN, aiming at a total force of 1.2 MN after cool-down which corresponds to the longitudinal electromagnetic forces at nominal current. In MQXFBP2, the longitudinal pre-stress target was 0.5 MN, consistent with MQXFA. Azimuthal loading is done by inserting increasingly larger interference keys in the key slots with the help of bladders while observing the shell vs. pole stress. In the first prototype, the average stress in the shell and coil was 70 and 90 MPa, respectively. The final pre-stress MQXFBP2 was 55 MPa in the shell and 80 MPa in the coil. The maximum spread in each longitudinal location is about 20 MPa.

One of the sources of stress variation along the length is the coil azimuthal size. With a coil size variation generally within ± 100 μm (see Fig. 7), the azimuthal stress at the winding pole is in a range of ± 20 MPa [26]. In order to prove the capability to control the stress variation along the length, a loading key with a conical shape to compensate coil geometry was tested in MQXFBMT2, a mechanical assembly test using non-conformed coils and the structure of MQXFBP2. Figure 9 shows that the average coil excess is around 200 μm larger in the center and compares the coil excess to the thickness of the conical loading key used in MQXFBMT2 to compensate coil geometry. The expected impact of replacing the 13.8 mm key by the conical key is an increase of the stress in the shell of 18 MPa in the magnet extremities whereas the stress in the center remains constant. The measured effect is very close to the expectations (see Fig. 9, bottom). The variable loading key method for controlling the stress along the length is described in detail in [27].

Magnetic measurements are an effective quality assurance tool that can detect small anomaly during the assembly process. They are performed at room temperature on the coil pack assembly, after centering the coil pack in the magnet structure and at the end of the loading using a rotating shaft [29]. Figure 10 compares the measurements after loading in the two prototype magnets. Measurements are within the target 3σ range assuming a 25 μm random error in the coil block positioning for non-allowed, and 100 μm for the allowed. Only the sextupole component in MQXFBP2 is above the targets, which will be corrected thanks to the use of magnetic shims [13]. The measured b_6 in MQXFBP1 is lower than the target of 0 units, consistent with the experience in the short models and MQXFA magnets ([19],[30]-[32][31]). Thanks to the iteration on the cross section, increasing the pole insulation thickness and re-

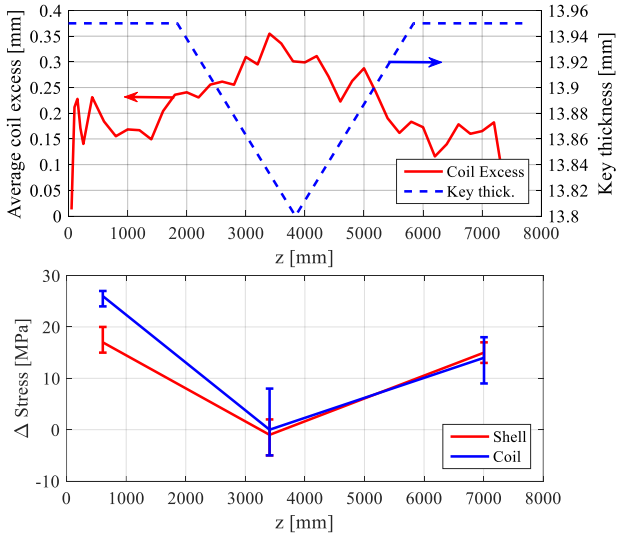

Fig. 9. Average azimuthal coil size deviation along the coil length and shape of the conical key in MQXFBMT2 to compensate coil geometry (Top). Change of stress in coil and shell when replacing the 13.8 mm key with the conical key in the three measuring locations (Bottom)

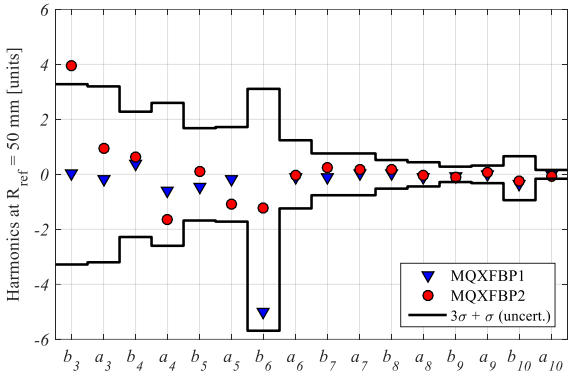

Fig. 10. Integral harmonics after loading in the two MQXFB prototype magnets compared with target field quality.

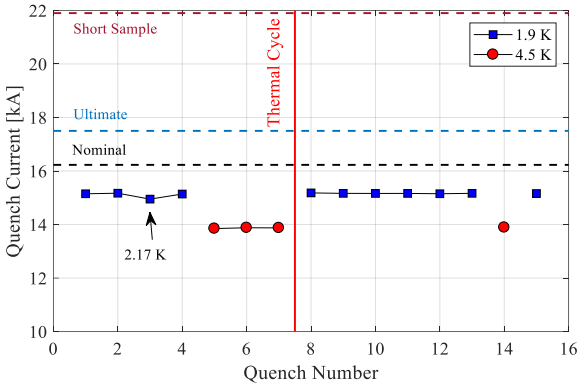

Fig. 12. Quench current of MQXFBP1. Data are compared to nominal, ultimate and short-sample current (estimated from witness samples).

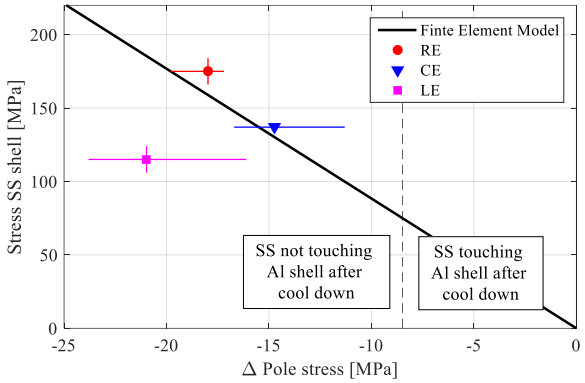

Fig 11. Measured stress in the stainless-steel shell after welding as a function of the increase of the stress in the coil with the welding.

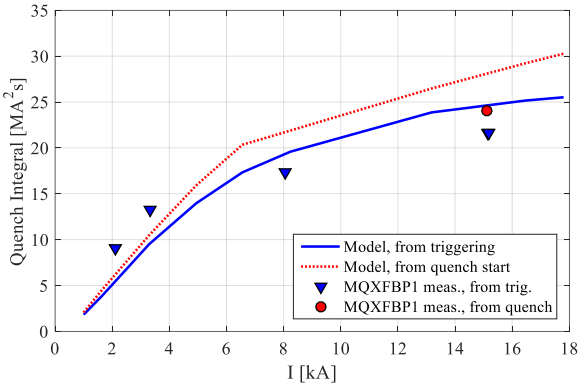

Fig. 13. Quench integral versus current computed with LEDET and measured in MQXFBP1.

ducing the mid-plane shim thickness by 0.125 mm, b_6 is close to the target in MQXFBP2. The difference in b_6 in between the two prototype magnets is 5 units, very close to the 5.3 units expected from simulations due to the change of cross section.

After loading, two 8-mm thick stainless-steel (SS) half shells are welded around the magnet. The cold mass assembly is completed with the welding of the end covers to the main cylinder formed by welded shells. Due to the impossibility to access the reverse side of the longitudinal weld of the shrinkage cylinders, a permanent backing strip has been chosen, in order to provide support for a fully penetrated root pass [31]. The target pre-stress in the SS shell is 75 MPa to assure that shell is still in contact with the magnet aluminum shell after cool-down. This corresponds to an increase of the coil stress of 8 MPa. The SS shells of the first prototype magnet were instrumented with strain gauges to validate welding parameters. Figure 11 shows that the measured stress in the shell is 100 to 175 MPa, corresponding to an increase of azimuthal stress in the coil of 15 to 20 MPa which was considered adequate for MQXFB magnets.

V. Cold Powering Tests

The first MQXFB prototype magnet was tested in summer 2020. The first quench at 1.9 K was at 15.1 kA, which corresponds to 70 % of the short sample current, comparable to the ones of MQXFS and MQXFA ([2],[7]). The magnet was blocked at this current level, with all the quenches in the same coil. At 4.5 K the quench current is 1 kA lower, corresponding to the same percentage of the load line (70 % of the short sample current). In all the cases, the quench starts in the magnet straight section. Quench propagation velocity at 15 kA is 15 m/s, similar to the typical quench propagation at this current level measured in short models and cable samples ([34],[35]), pointing to a local defect and not a global degradation of the coil. When increasing the ramp rate, the quench current does not increase as observed MQXFS3 and MQXFAP1b[7]. After thermal cycle, quench current and location did not change showing a very systematic behaviour.

Mechanical measurements on the stainless steel shell confirmed that the decrease on azimuthal pre-stress in the He-vessel during cool down is 75 MPa. In the axial direction, the longitudinal loading system carries only 5% of the electromagnetic forces during powering, with a total rods elongation of 0.6 mm, consistent with expecations [22]. The magnet passed all high voltage test, including the insulation test quench heater to coil at 850 V, 100 K and 1 bar [41].

A. Protection

The protection strategy relays on outer layer quench heaters and CLIQ [36], and has been validated on short models without energy extraction [37], and on US prototypes with energy extraction [38]. The simultaneous use of CLIQ and quench heaters gives a quench load (from quench start) in

TABLE I. INTEGRAL TRANSFER FUNCTION (T/KA)

	MQXFBP1	Reference Design	Ref. design including radial deformation
After loading	63.394	63.400	63.424
80 K	63.754	63.206	63.661
13.6 kA	59.192	58.372	58.956

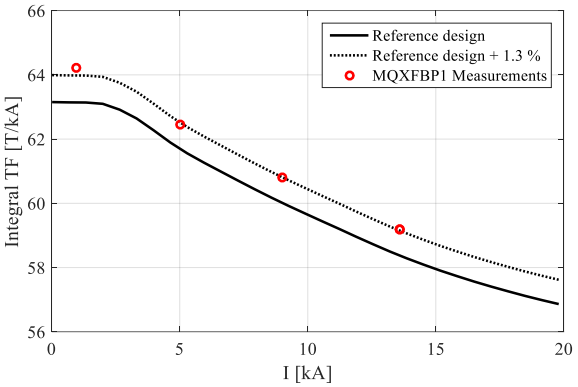

Fig. 13. Integral transfer function versus current computed with ROXIE and measured in MQXFBP1.

MQXFBP1 of 25 MIITs at 15.1 kA, corresponding to a hotspot temperature of 170 K. Figure 13 compares the measured quench load from quench start and from protection triggering of MQXFBP1 and the expected quench load computed with LEDET [39]. The quench load from the protection triggering in MQXFBP1 at 15.1 kA is ~ 22 MIITs, which is 10 % lower than expected.

B. Integral field

The magnetic transfer function (TF) is defined as the ratio between the gradient and the magnet current. Table I summarizes the integral transfer function at room temperature, after room temperature loading, at 80 K and at 13.6 kA. The integral field is 1.3 % larger than the reference design which does not include the impact of radial coil deformations due to loading and cool down (see Fig. 13). This is consistent with the short model magnets experience [40]. Around 1 % of the discrepancy is coming from the increase of field due to the radial deformation during cool down and powering, not included in the original design. The remaining 0.3 % is due to a mismatch between the nominal and actual magnet length. The nominal reference of MQXF magnets has been decreased from 16.47 kA to 16.23 kA to account for the feedback from the measurements. The ultimate current decreased by 400 A, from 17.89 kA to 17.50 kA, since the original estimate accounted for ~1% larger values with respect to the energy scaling from 7 to 7.5 TeV. The nominal gradient decreased from 132.6 T/m to 132.2 T/m and the peak field in the coil from 11.4 T to 11.3 T.

VI. CONCLUSIONS

The development of the MQXFB quadrupole magnets for the HL-LHC project is moving towards the completion of the prototype phase and is advancing in the series one. So far, 14 conformed MQXFB coils have been manufactured, the first prototype has been tested and the assembly of the second prototype is completed. Conductor procurement is close to completion and coil fabrication resumed after and in-depth review of the manufacturing process with a production rate of one coil per month. The coil manufacturing is driving the schedule production rate. A production line of one winding machine, one reaction oven and one impregnation system can produce coil in about 5 months. The plan for 2021 is to manufacture the first two series magnets, MQXFB01 and MQXFB02.

The first prototype MQXFBP1 was limited in performance reaching a current of 15.1 kA, equivalent to 6.5 TeV operation in the LHC. The quench corrent at 4.5 K is 1 kA lower, correponding to 70 % of the short sample limit at both temperature levels. There are not traces of reverse or erratic behaviour as is MQXFS3 and MQXFAP1b [2]. Magnet disassembly is on-going to underatnd the origin of the performance limitation. The assembly of the second prototype is completed and the test is planned for beginning of 2021.

ACKNOWLEDGMENTS

The authors wish to thank the technical staff for the construction and cold powering test of the magnet.

REFERENCES

[1] O. Bruning, et al. 2002 LHC Project Report 626
[2] E. Todesco, et al., “The HL-LHC interaction region magnets towards series production”, submitted for publication.
[3] P. Ferracin et al., “Magnet design of the 150 mm aperture low-β quadrupoles for the high luminosity LHC,” IEEE Trans. Appl. Supercond., vol. 24, no. 3, Jun. 2014, Art. no. 4002306.
[4] P. Ferracin, et al., “Development of MQXF: The Nb_3Sn low-β quadrupole for the Hilumi LHC,” IEEE Trans. Appl. Supercond., vol. 26, no. 4, Jun. 2016, Art. no. 4000207.
[5] G. Ambrosio, et al., “Lessons learned from the prototypes of the MQXFA Low Beta Quadrupoles for HL-LHC and plans for production in the US,” IEEE Trans. Appl. Supercond., aubmitted for publication.
[6] S. A. Gourlay et al., “Magnet R&D for the US LHC accelerator research program,” IEEE Trans. Appl. Supercond., vol. 16, no. 2, pp. 324–327, Jun. 2006.
[7] P. Ferracin, et al., “The HL-LHC Low-β Quadrupole Magnet MQXF: From Short Models to Long Prototypes,” IEEE Trans. Appl. Supercond., vol. 29, no. 5, Aug. 2019, Art. no. 4001309.
[8] B. Bordini, et al., “The bundle-barrier PIT wire developed for the HiLumi LHC project,” IEEE Trans. Appl. Supercond., vol. 27, no. 4, Jun. 2017, Art. no. 6000706.
[9] B. Bordini, et al., “The Nb_3Sn superconductor procured for the High Luminosity Upgrade of the Large Hadron Collider., submitted for publication.
[10] J. Fleiter, et al., “Characterization of Nb3Sn Rutherford Cable Degradation Due to Strands Cross-Over,” IEEE Trans. Appl. Supercond., vol. 28, no. 4, Jun. 2018, Art. no. 4802205.
[11] J. Fleiter, et al., “Optimization of Nb3Sn Rutherford Cables Geometry for the High-Luminosity LHC,” IEEE Trans. Appl. Supercond., vol. 27, no. 4, Jun. 2017, Art. no. 4004305.
[12] E. F. Holik et al., “Fabrication and Analysis of 150 mm Aperture Nb_3Sn MQXF Coils,” *IEEE Trans. Appl. Supercond.*, vol. 26, no. 4, Jun. 2016, Art. no. 4000907.
[13] S. Izquierdo Bermudez et al., “Second-generation coil design of the Nb3 Sn low-β quadrupole for the high luminosity LHC,” vol. 26, no. 4, Jun. 2016, Art. no. 4001105.

[14] F. Lackner *et al*., "Status of the Long MQXFB Nb3 Sn coil prototype production for the HiLumi LHC," *IEEE Trans. Appl. Supercond.*, vol. 27, no. 4, Jun. 2017, Art. no. 4002605.

[15] F. Lackner *et al*., "Fabrication of the 7.3-m-Long Coils for the Prototype of MQXFB, the Nb3Sn Low-b Quadrupole Magnet for the HiLumi LHC," *IEEE Trans. Appl. Supercond.*,

[16] J. Axensalva, *et al*., "Vacuum Pressure Impregnation Setup at CERN for Nb_3Sn Coils," *IEEE Trans. Appl. Supercond.*, vol. 30, no. 4, June 2020, Art. no. 4003204.

[17] F. Rodriguez Mateos, *et al*, "Electrical design criteria for the HL-LHC inner triplet magnets," CERN Engineering Specification, EDMS 1963398.

[18] J. F. Troitino et al., "Applied metrology in the production of superconducting model magnets for particle accelerators," IEEE Trans. Appl. Supercond., vol. 28, no. 3, Apr. 2018, Art. no. 4002106.

[19] S.Izquierdo Bermudez, et al., "Geometric Field Errors of Short Models for MQXF, the Nb_3Sn Low-β Quadrupole for the High Luminosity LHC," *IEEE Trans. Appl. Supercond.*, vol. 28, no. 3, April. 2018, Art. no. 4006306.

[20] E. Takala, et al., "Preload Characterization of Short Models of MQXF the Nb_3Sn Low-β Quadrupole for the Hi-Lumi LHC," *IEEE Trans. Appl. Supercond.*, vol. 30 no. 4, April. 2020, Art. no. 4002806.

[21] G. Vallone et al., "Mechanical performance of short models for MQXF, the Nb3 Sn low-β quadrupole for the hi-lumi LHC," IEEE Trans. Appl. Supercond., vol. 27, no. 4, Jun. 2017, Art. no. 4002906.

[22] H. Pang et al., "Mechanical design studies of the MQXF long model quadrupole for the HiLumi LHC," IEEE Trans. Appl. Supercond., vol. 27, no. 4, Jun. 2017, Art. no. 4004105.

[23] G. Vallone et al., "Mechanical design analysis of MQXFB, the 7.2-m-long low-β quadrupole for the high-luminosity LHC upgrade," IEEE Trans. Appl. Supercond., vol. 28, no. 3, Apr. 2018, Art. no. 4003705.

[24] G. Vallone et al., " Assembly of MQXFBP1, mechanical model of the 7.2 m long low-β quadrupole for the high luminosity LHC upgrade," IEEE Trans. Appl. Supercond., to be published.

[25] G. Vallone et al., "Mechanical analysis of the short model magnets for the Nb3 Sn low-β quadrupole MQXF," IEEE Trans. Appl. Supercond., vol. 28, no. 3, Apr. 2018, Art. no. 4003106.

[26] G. Vallone et al., "Summary of the mechanical performances of the 1.5 long models of the Nb3Sn low-β quadrupole MQXF," IEEE Trans. Appl. Supercond., vol. 29, no. 9, Aug. 2019, Art. no. 4002805.

[27] G. Vallone and P. Ferracin, "Modeling coil-pole debonding in Nb3Sn superconducting magnets for particle accelerators," IEEE Trans. Appl. Supercond., vol. 27, no. 8, Dec. 2017, Art. no. 4004611.

[28] E. Takala, *et al*., "Preload characterization of prototypes of MQXFB the long Nb3Sn Low-β Quadrupole for the Hi-Lumi LHC," IEEE Trans. Appl. Supercond., submitted for publication.

[29] P. Rogacki, L. Fiscarelli, S. Russenschuck and K. Hameyer, "A Rotating-Coil Scanner for the Precise Magnetic Characterization of Superconducting Accelerator Magnets at Ambient Temperature," in *IEEE Transactions on Magnetics*, doi: 10.1109/TMAG.2020.3005722.

[30] L. Fiscarelli, et al., "Magnetic measurements on the first CERN-built models of the insertion quadrupole MQXF for HL-LHC," IEEE Trans. Appl. Supercond., vol. 28, no. 3, Apr. 2018, Art. no. 4002605.

[31] X. Wang, et al., "Field Quality Measurement of a 4.2-m-Long Prototype Low-β Nb3Sn Quadrupole Magnet During the Assembly Stage for the High-Luminosity LHC Accelerator Upgrade Project," IEEE Trans. Appl. Supercond., vol. 29, no. 5, Aug. 2019, Art. no. 4007006.

[32] S. Izquierdo Bermudez *et al*., "Magnetic Analysis of the MQXF Quadrupole for the High-Luminosity LHC," in *IEEE Transactions on Applied Superconductivity*, vol. 29, no. 5, pp. 1-5, Aug. 2019, Art no. 4901705, doi: 10.1109/TASC.2019.2897848

[33] Jose Luis Rudeiros, et al, "Structural Analysis of WP3 Q2 LMQXFB Triplet Cold Masses," CERN Internal Note, EDMS 2363726.

[34] J. Fleiter, et al, "Quench Propagation in Nb_3Sn Rutherford Cables for the Hi-Lumi Quadrupole Magnets," *IEEE Trans. Appl. Supercond.*, vol. 25, no. 3, Aug. 2015, Art. no. 4802504.

[35] J. Ferradas Troitino, et al, " 3-D Thermal-Electric Finite Element Model of a Nb_3Sn Coil During a Quench," *IEEE Trans. Appl. Supercond.*, vol. 29, no.5, Aug. 2019, Art. no. 4701306.

[36] E. Ravaioli, et al, "Quench Protection System Optimization for the High Luminosity LHC Nb_3Sn Quadrupoles," IEEE Trans. Appl. Supercond., vol. 27, no. 4, Junr. 2017, Art. no. 4702107.

[37] E. Ravaioli, et al, "Quench Protection Performance Measurements in the First MQXF Magnet Models," IEEE Trans. Appl. Supercond., vol. 28, no. 3, Aug. 2018, Art. no. 4701606.

[38] E. Ravaioli, et al, "Quench protection of the first 4 m long prototype of the HL-LHC Nb3Sn quadrupole magnet," IEEE Trans. Appl. Supercond., vol. 29, no. 5, Aug. 2019, Art. no. 4001309.

[39] E. Ravaioli, , et al, "Quench Protection Studies for the High Luminosity LHC Nb3Sn Quadrupole Magnets," *IEEE Trans. Appl. Supercond.*, submitted for publication.

[40] S. Izquierdo Bermudez, et al., "Magnetic Analysis of the MQXF Quadrupole for the High-Luminosity LHC," IEEE Trans. Appl. Supercond., vol. 29, no. 5, Aug. 2019, Art. no. 4901705.

[41] M. Baldini, et al., "Assessment of MQXF Quench Heater Insulation Strength and Test of Alternative Design", *IEEE Trans. Appl. Supercond.*, submitted for publication.